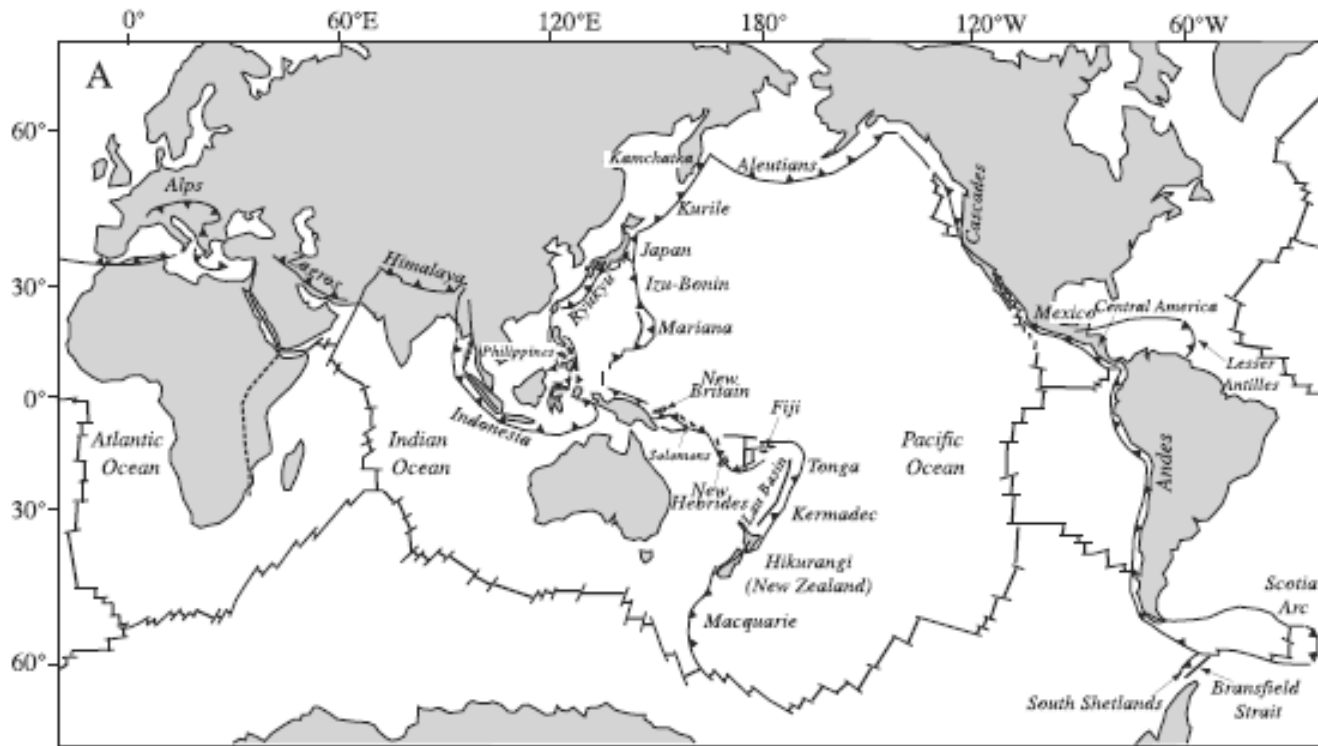# Ocean-Continent and Ridge Subduction

Oluwaseun Fadugba

*Seismotectonics 2016*
CERI

Motivation

Figure 1. Subduction zones and convergent plate margins. (a) Location of convergent plate margins on Earth (modified after *Lallemand* [1999]). Active back arc basins are also shown. (b) Schematic section through the upper 140 km of a subduction zone, showing the principal crustal and upper mantle components and their interactions. Note that the location of the "mantle wedge" (unlabeled) is that part of the mantle beneath the overriding plate and between the trench and the most distal part of the arc where subduction-related igneous or fluid activity is found. MF stands for magmatic front. (c) Schematic section through the center of the Earth, which shows better the scale of subduction zones. Subducted lithosphere is shown both penetrating the 660 km discontinuity (right) and stagnating above the discontinuity (left). A mantle plume is shown ascending from the site of an ancient subducted slab. Dashed box shows the approximate dimensions of the shallow subduction zone of Figure 1b.
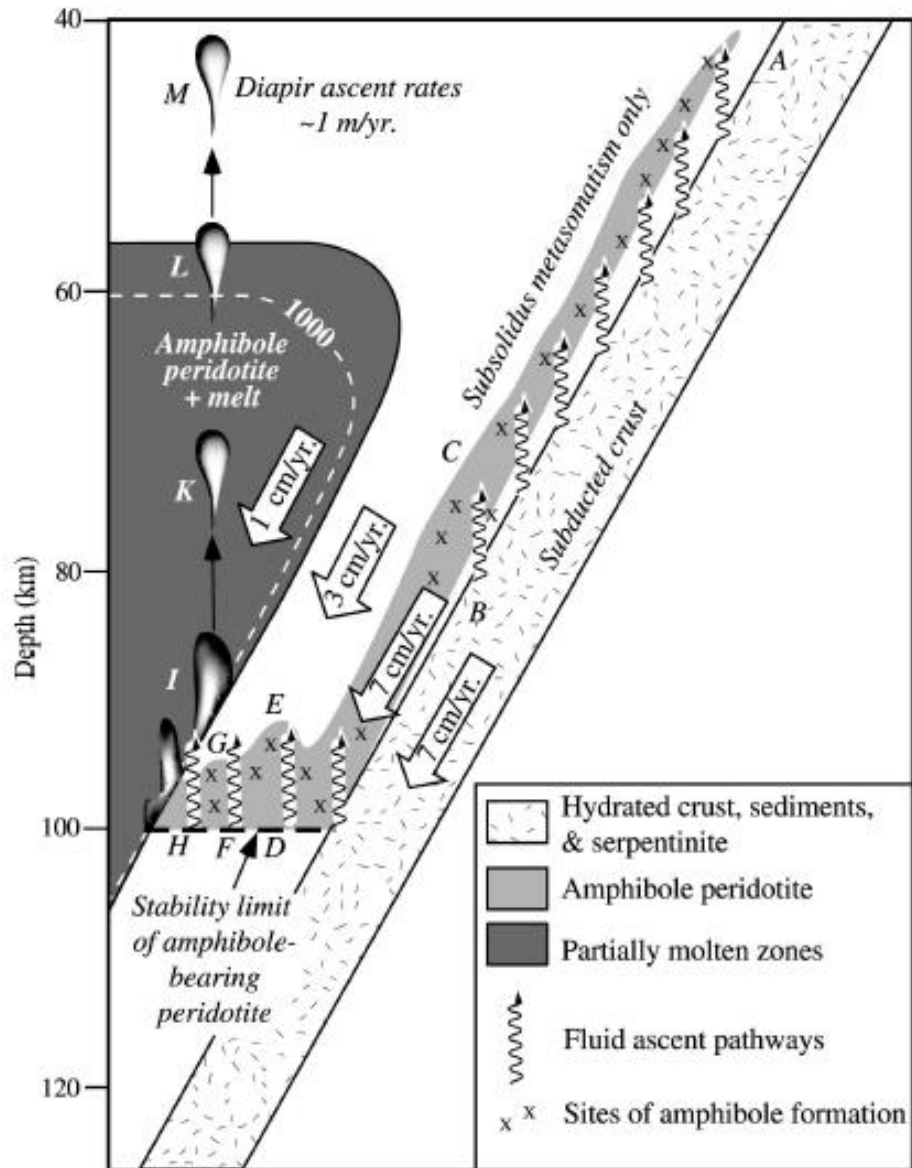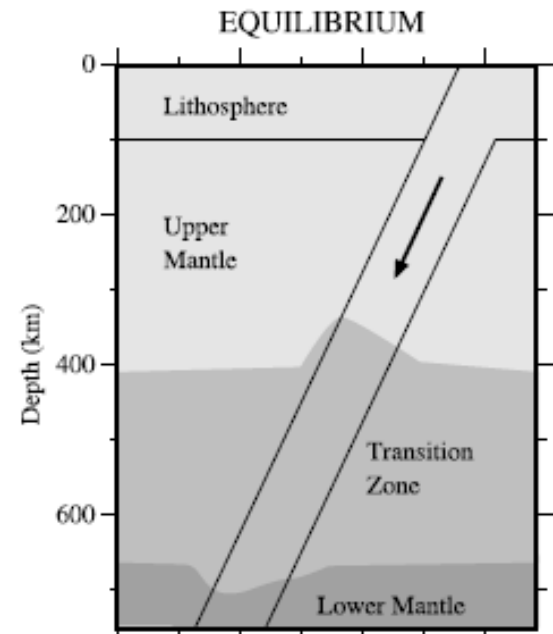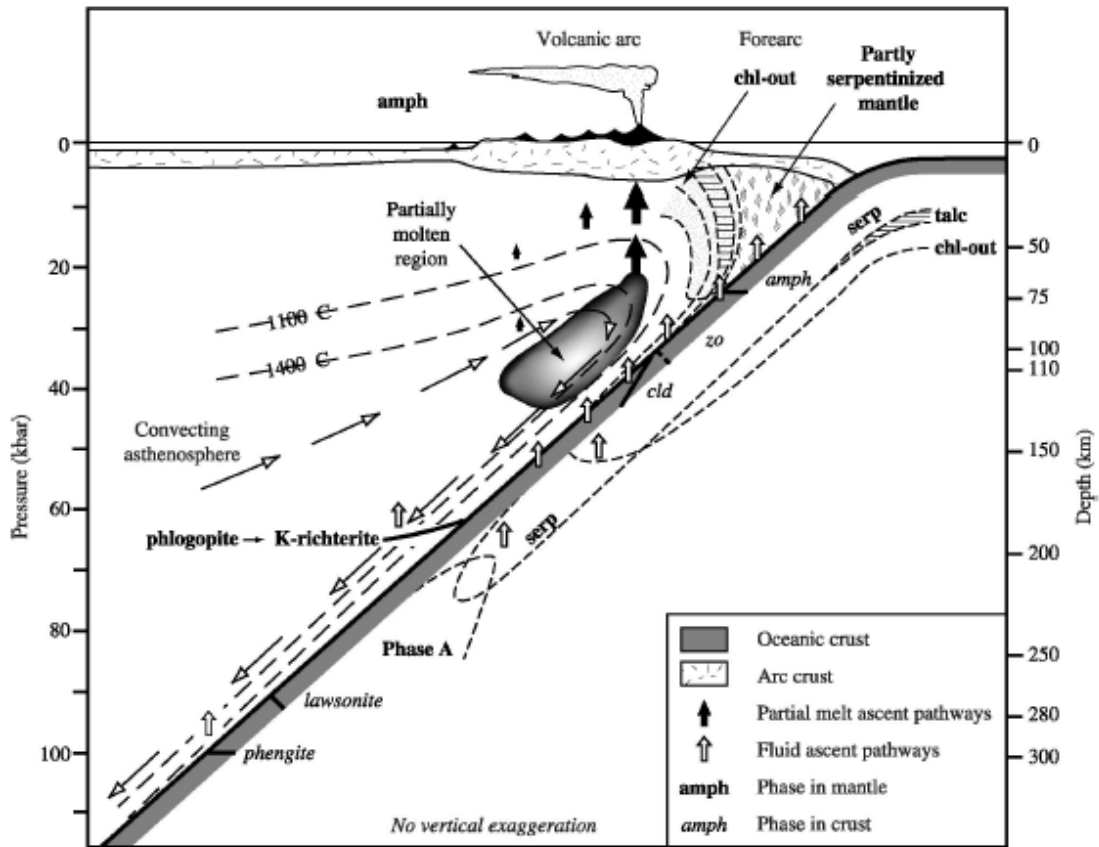
(Stern, 2002)

Motivation
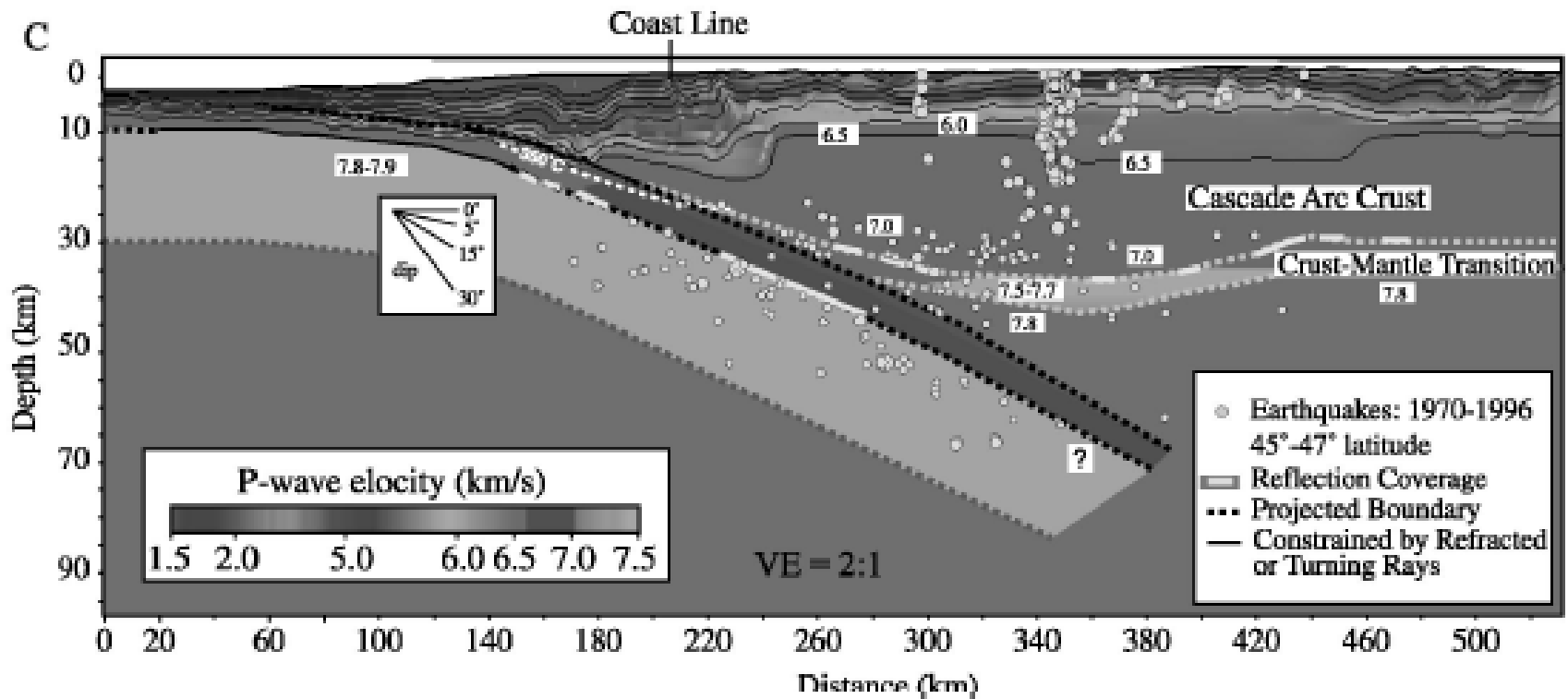
(Stern, 2002)

Motivation

(Stern, 2002)

Motivation

Figure 9. Model for dehydration of subducted materials (modified after *Schmidt and Poli* [1998]). Dehydration of subducted peridotite and oceanic crust occurs continuously to ~150–200 km; thus water is continuously supplied to the overlying mantle. The shaded region in the mantle wedge labeled "partially molten region" is expected to melt to a significant degree. The volcanic front forms where the amount of melt can separate and rise to the surface. Open arrows indicate rise of fluid, solid arrows indicate rise of melts. Long arrows indicate flow of asthenosphere in the mantle wedge. Stippled area marks stability field of amphibole beneath the forearc. Dashed lines outline stability fields of hydrous phases in peridotite. The horizontally ruled region shows where talc is stable. For some thermal structures a portion of the peridotitic lithosphere will be <600°C at 62 kbar; serpentine will react to "phase A," and thus H₂O will be subducted to large depth. In the oceanic crust, temperatures can be low enough to preserve lawsonite and phengite to their maximum pressure stability; however, at somewhat warmer conditions (slower subduction, shallower angle, and younger crust), zoisite (zo) will be the last potassium-free phase to decompose, and the top of the oceanic crust (phengite-rich sedimentary layer) might melt. Single-phase transitions, which cause a potassium-rich fluid pulse, could result from the breakdown of phengite in oceanic crust and from the phlogopite to K-richterite reaction in K-metasomatized mantle. Chl stands for chlorite; Cld stands for chloritoid.
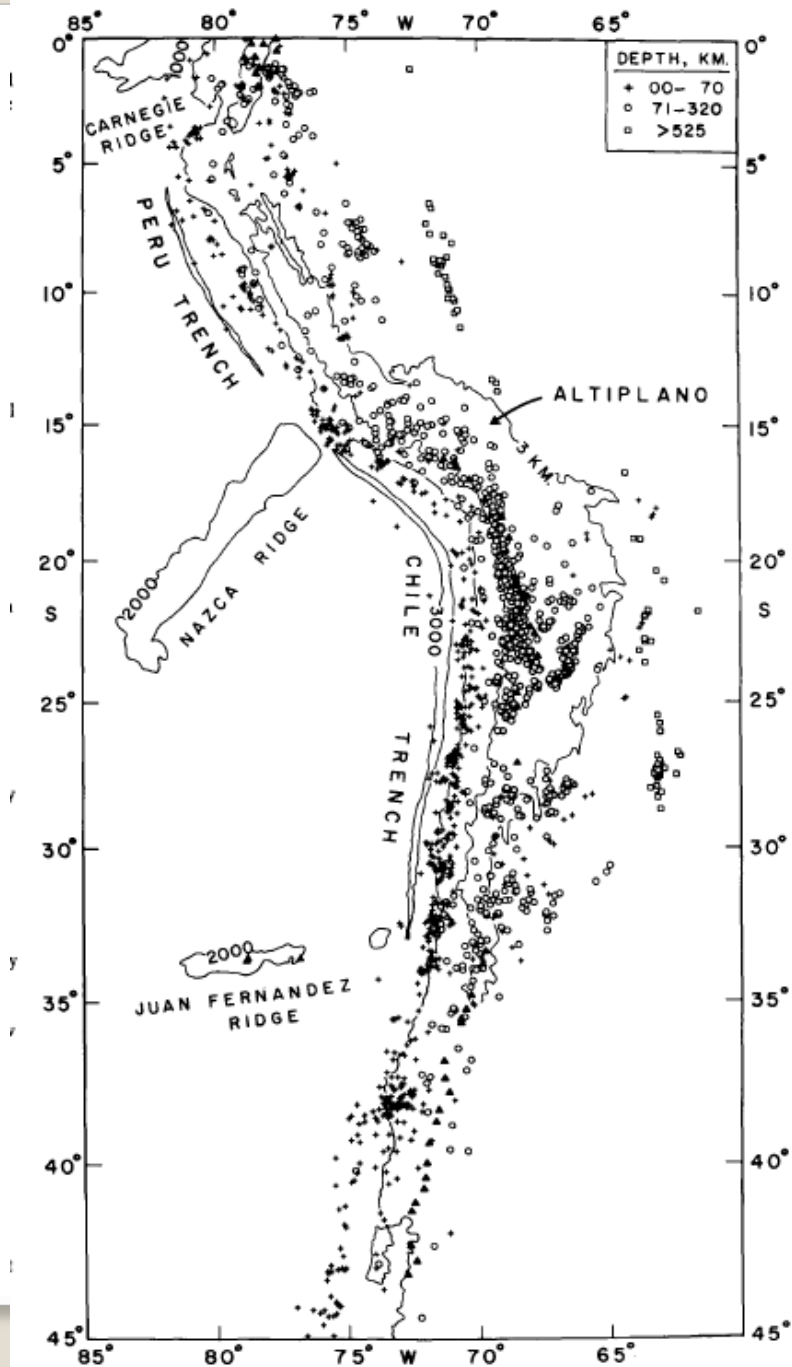
(Stern, 2002)

Spatial distribution of earthquakes and subduction of the Nazca plate beneath South America

Muawia Barazangi,* Bryan L. Isacks

Department of Geological Sciences, Cornell University
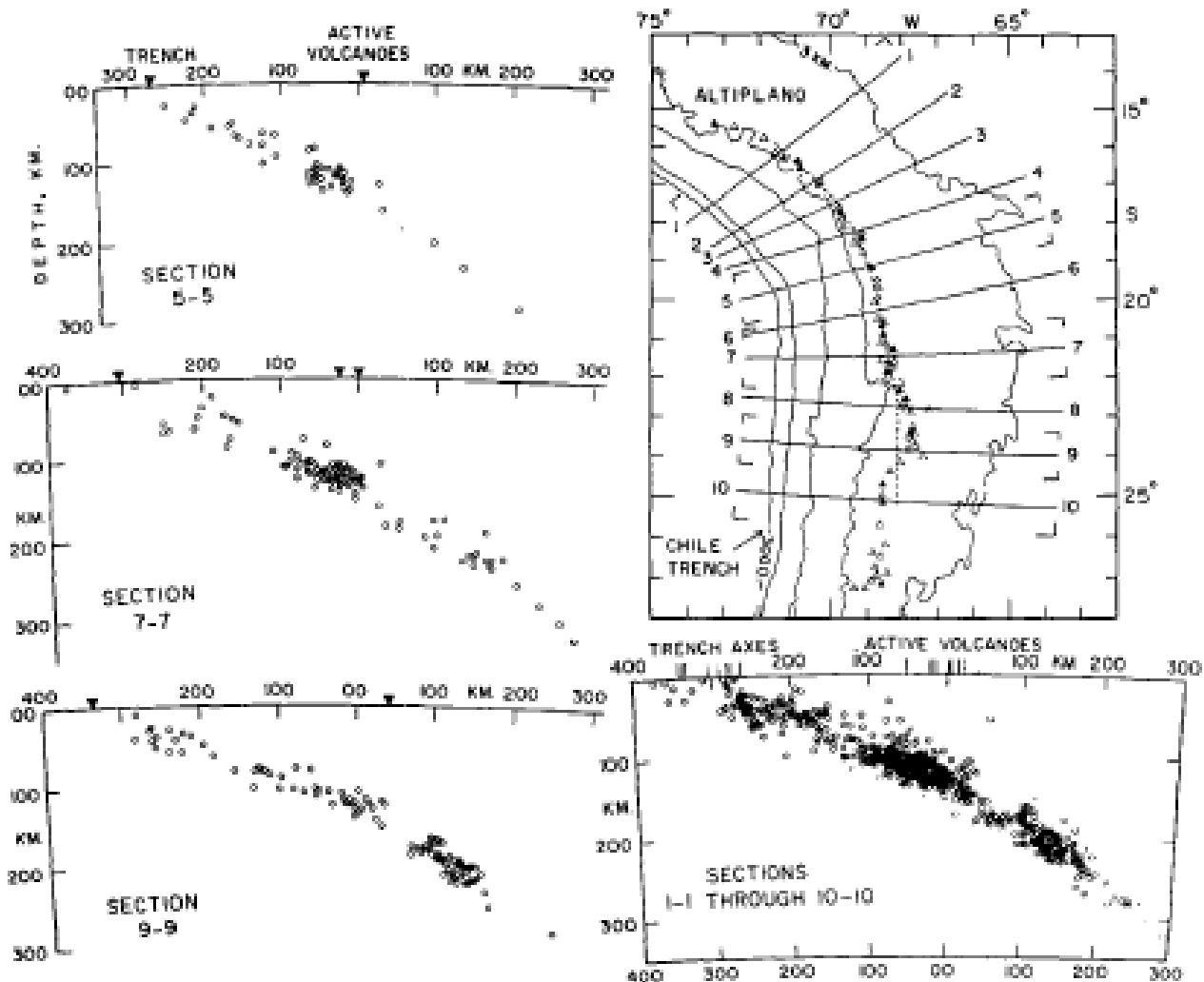
Ithaca, New York 14853

Seismicity map of South America

Figure 2. Map of southern Peru–northern Chile region, showing location of 10 cross sections superimposed to obtain composite section shown in lower right-hand corner. Projection of volcanoes and trench axes shown by vertical lines on composite section. Three representative sections are shown on left side. Solid triangles = historical volcanoes; open trianges = Quaternary volcanoes (from Zeil, 1964; Bullard, 1962).
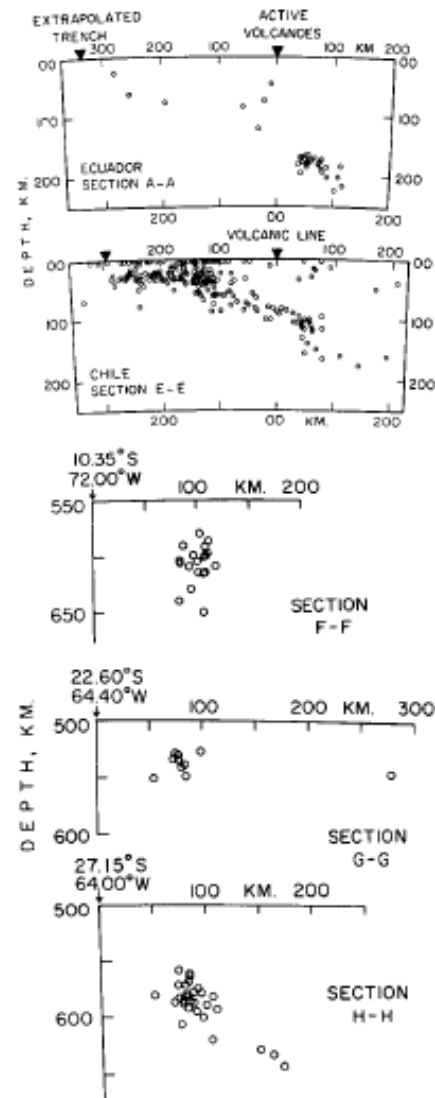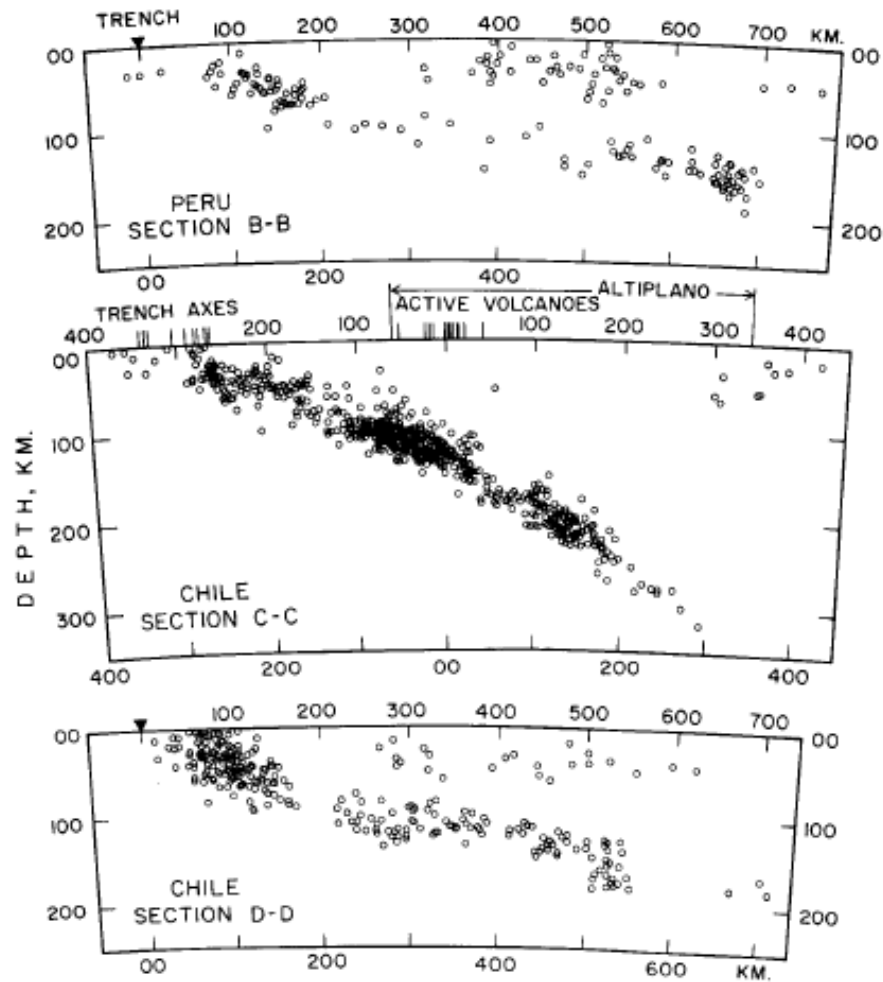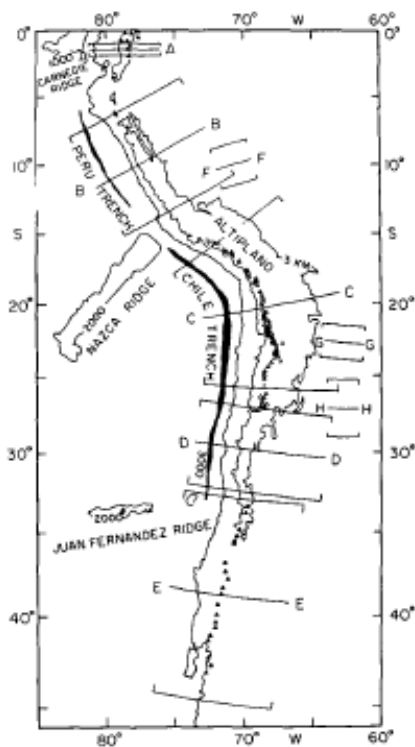
Figure 4. Cross sections showing segments of inclined seismic zone (A, B, C, D, E) and deep seismic zone (F, G, H). See Figure 3 for locations and limits of sections.
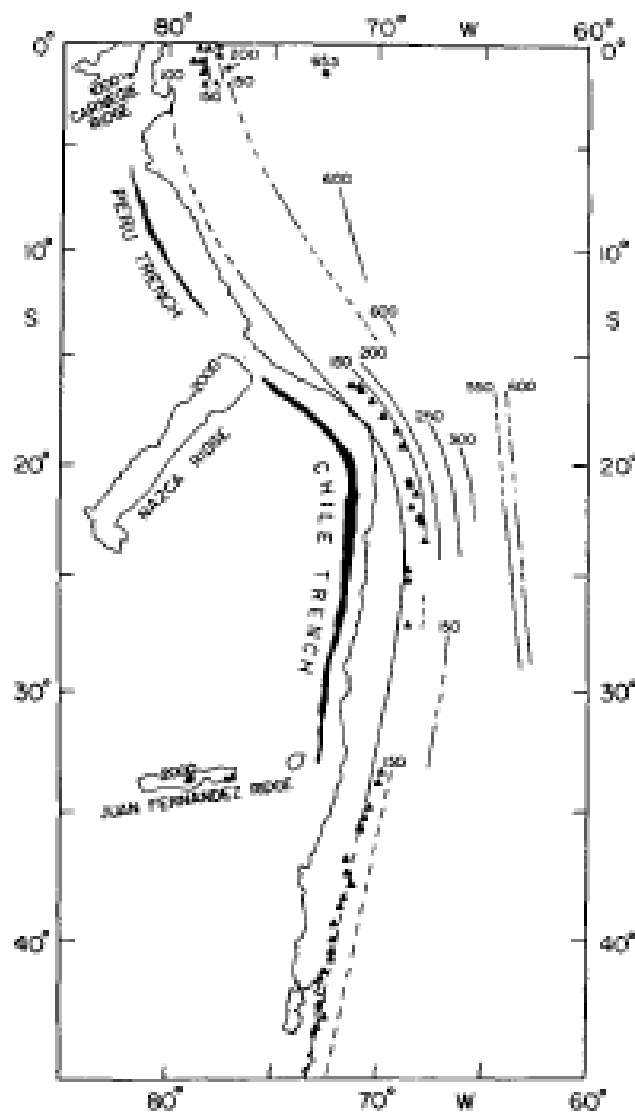
Figure 5. Map showing contours of hypo-central depth to top of inclined seismic zone. Dashed lines indicate that contours are based on fewer data than those shown by solid lines.
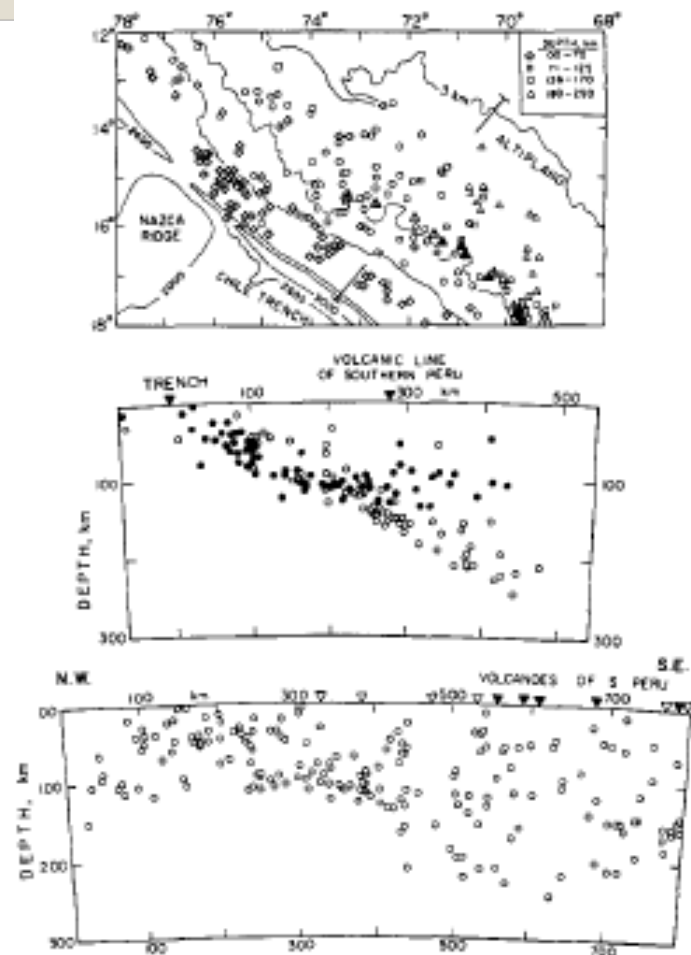

Figure 6. Map view, cross section, and longitudinal section of distribution of earthquakes in southern Peru and northern Chile, showing abrupt increase in hypocenter depth in passing from flat Peru segment to more steeply dipping northern Chile segment. Filled and open circles in middle cross section are for events to northwest and southeast, respectively, of line indicated in map view. Longitudinal section is perpendicular to that line. Solid triangles = historical volcanoes; large open triangles (and divided triangles in map view) = Quaternary volcanoes.

Subduction of the Chile Ridge: Upper mantle structure and flow
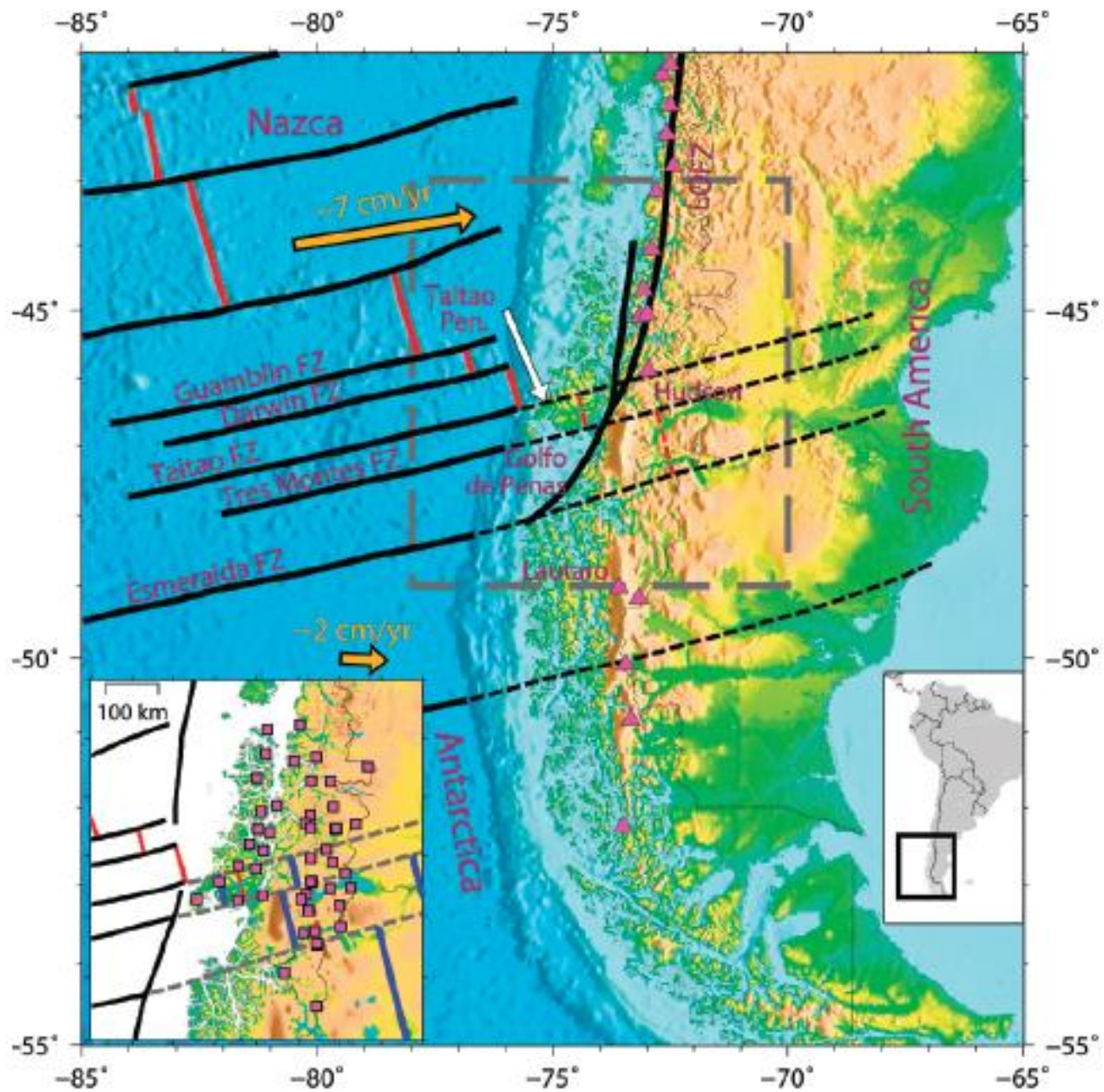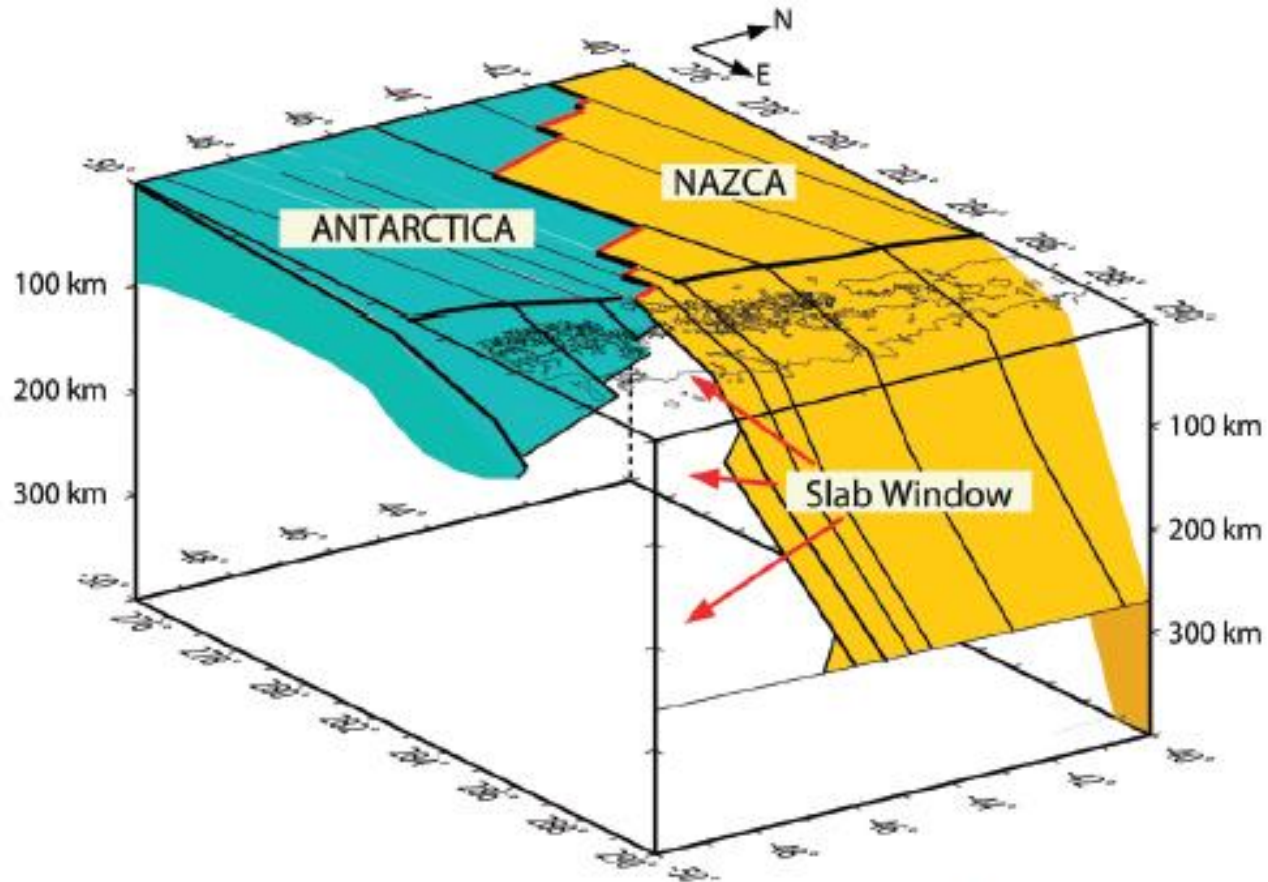
Figure 2. Development of slab windows, as projected from Chile Ridge surface structure and magnetic anomalies (e.g., Fig. 3) (Murdie and Russo, 1999). Separation of the trailing edge of the Nazca plate and the leading edge of the Antarctic plate opens a slab window once ambient temperatures are high enough to prevent lithosphere formation.

Map of P-wave velocity Anomalies
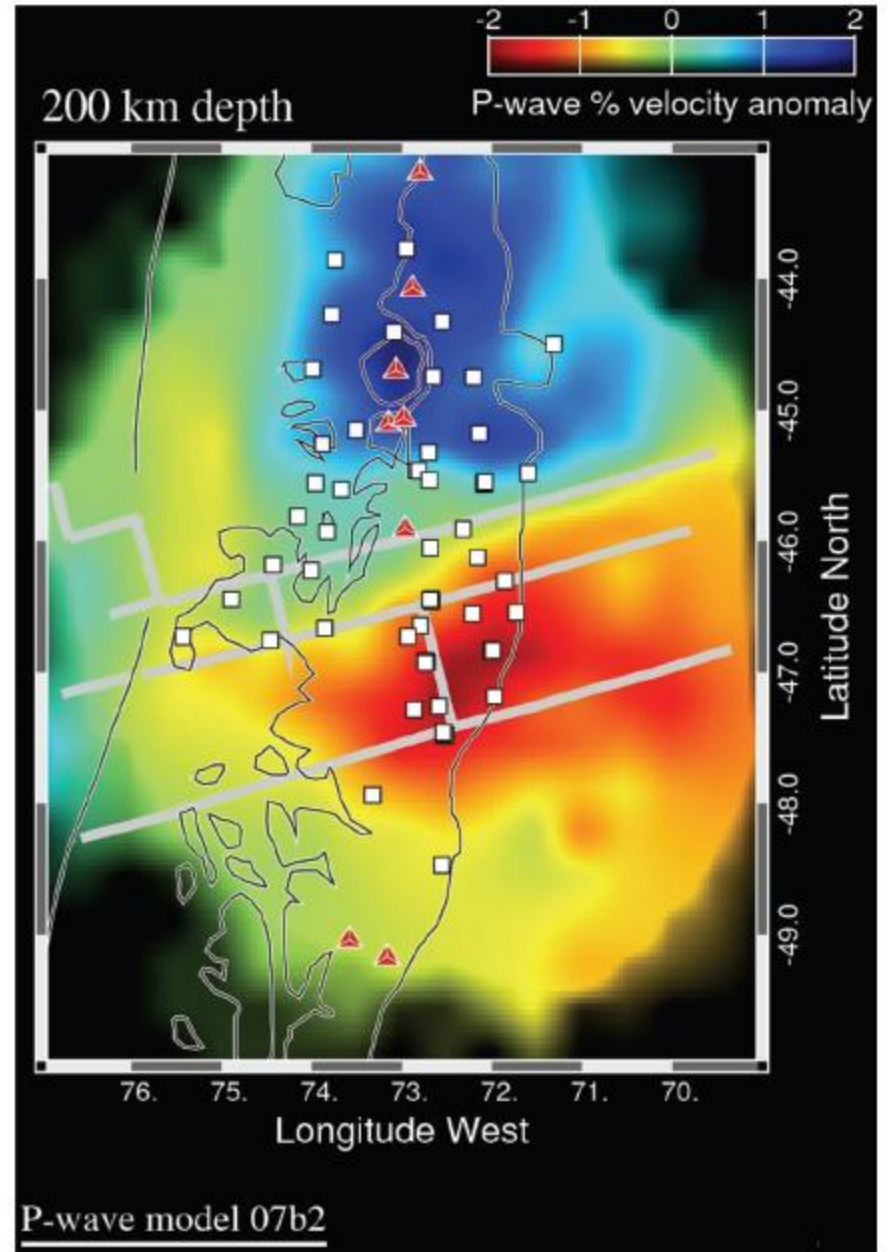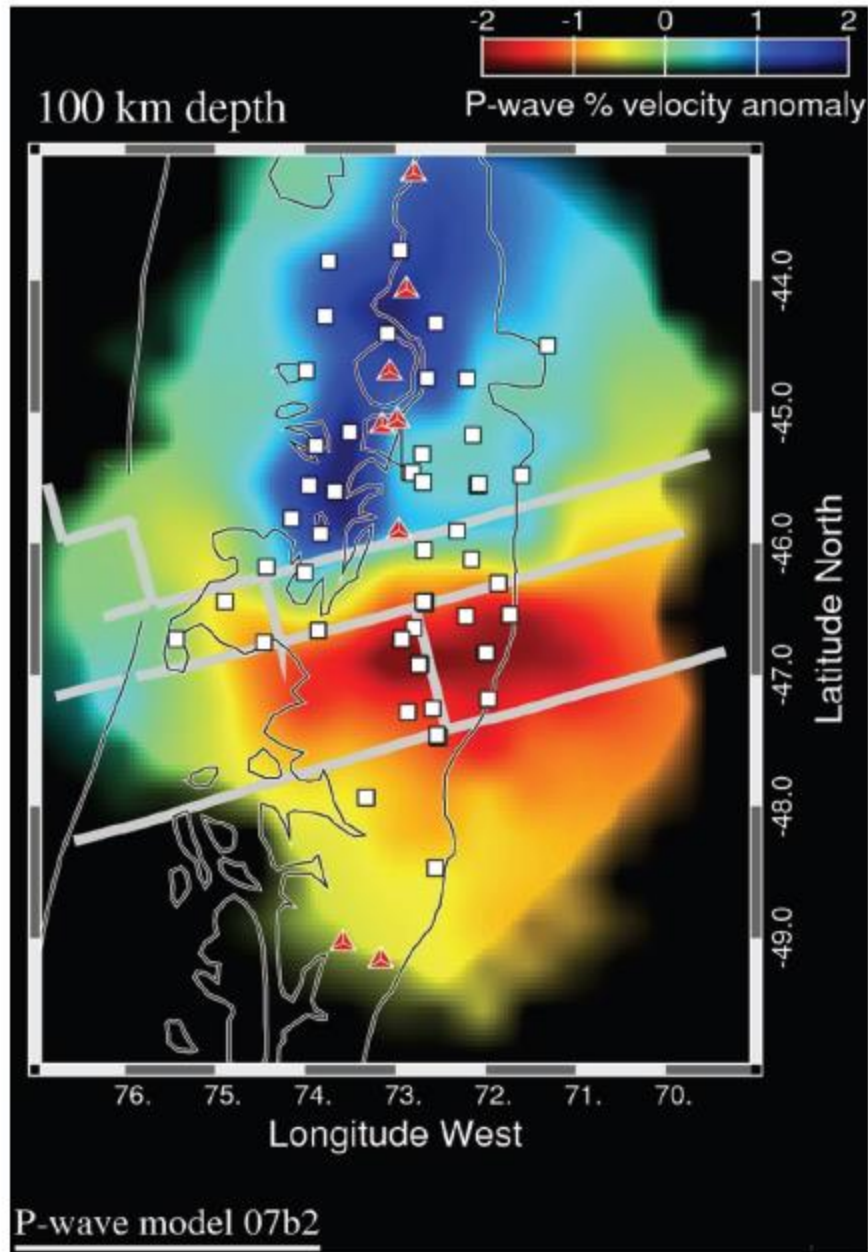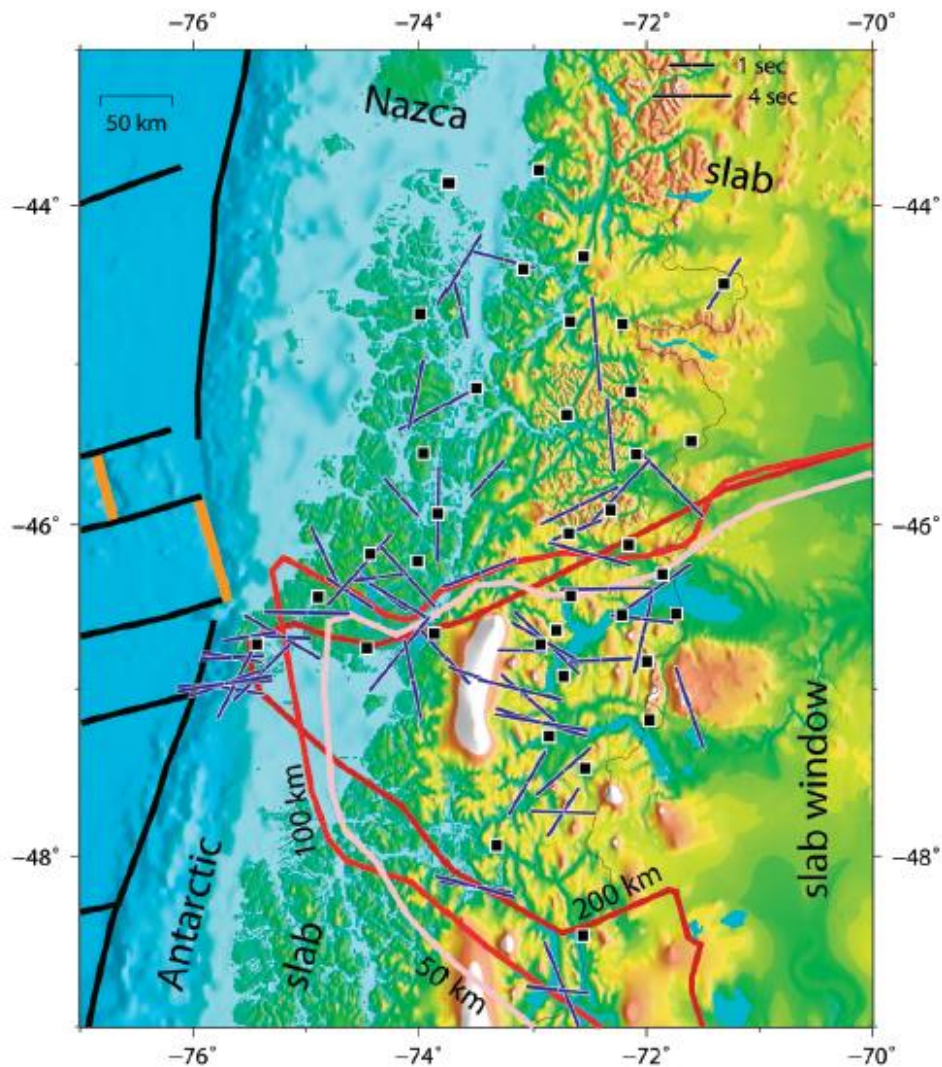
Figure 4. Map of shear wave splitting measurements. Blue bars trend in the fast polarization direction; lengths are proportional to delay times. Fast trends are variable, but splitting delays are uniformly high (mean = 2.98 s), which is near the global maximum for teleseismic splitting. Strong, variable splitting indicates a variable upper mantle flow field beneath South America and the subducted Nazca and Antarctic slabs. Patagonian slab window boundary defined by P-wave tomography (Fig. 3), shown at three depths: heavy pink, red, and dark red lines.

Figure 5. Schematic 3-D block diagram of upper mantle flow in the vicinity of the slab window delineated by the travel time inversions 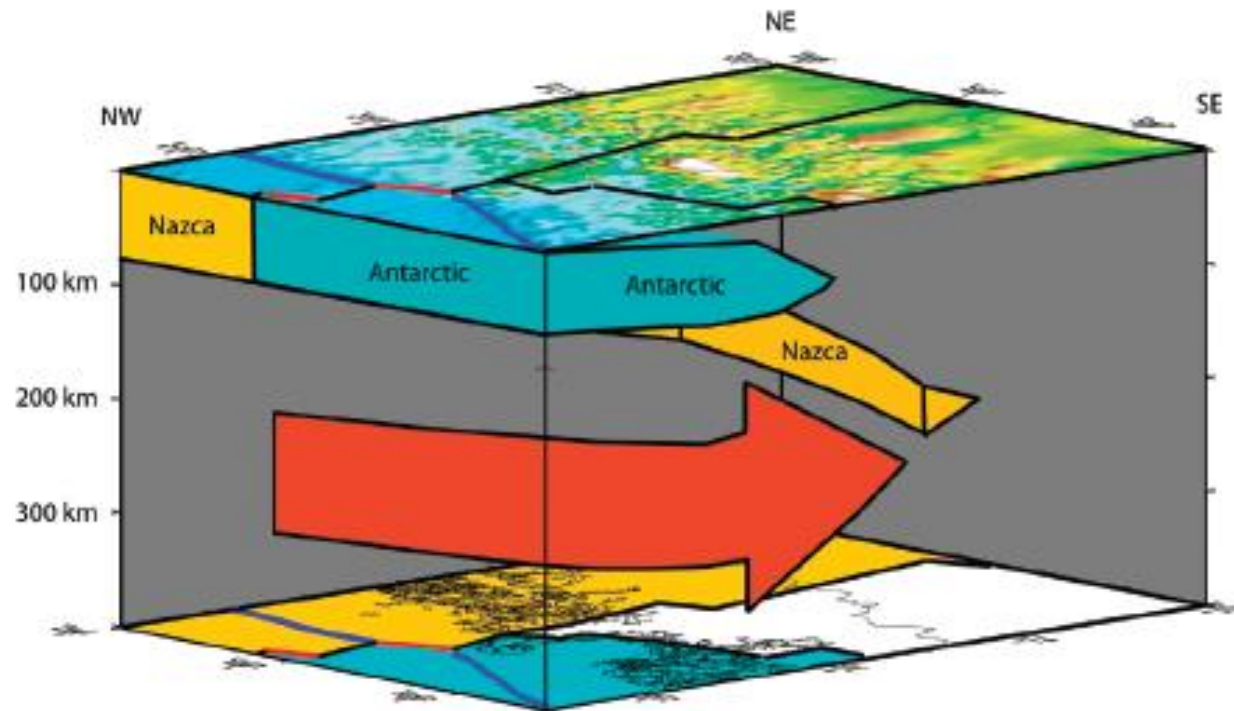(Fig. 3); view from SW. Top map shows relief and locations of Chile Ridge structures before and after subduction. Bottom shows coastline and Chile Ridge structures over color-coded slab plates: Nazca plate—yellow; Antarctic plate—blue-green; same colors for portions of the slab visible in the block diagram itself. Red arrow generally parallels shear-wave splitting fast trends and upper mantle flow in the vicinity of the slab window opening. The northern, shallower portion of the slab window is not visible from this viewpoint.

Andean tectonics related to geometry of subducted Nazca plate

TERESA E. JORDAN
BRYAN L. ISACKS
RICHARD W. ALLMENDINGER   } *Department of Geological Sciences, Cornell University, Ithaca, New York 14853*
JON A. BREWER*
VICTOR A. RAMOS   *Servicio Geologico Nacional, Buenos Aires, Argentina*
CLIFFORD J. ANDO*   *Department of Geological Sciences, Cornell University, Ithaca, New York 14853*
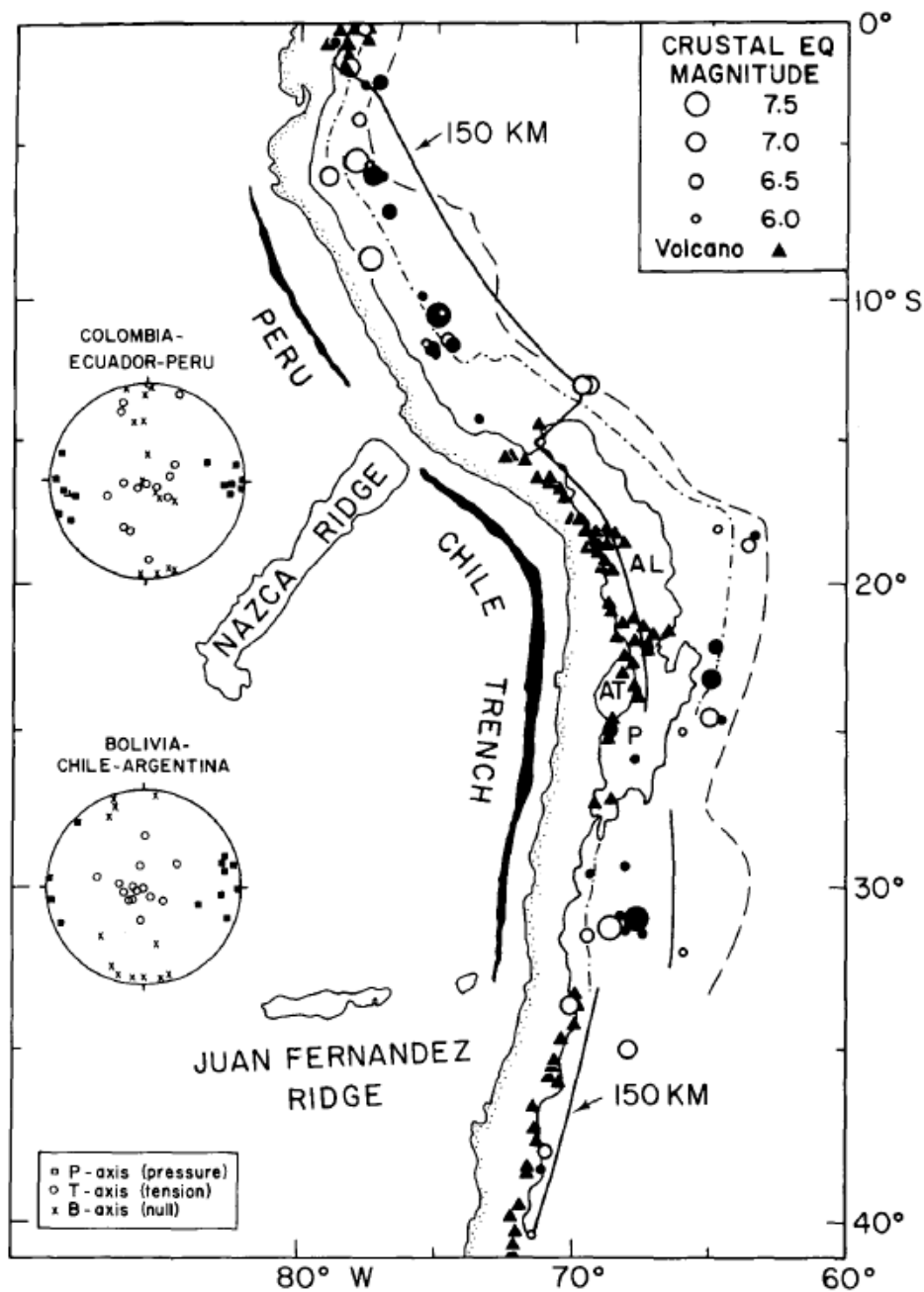
Figure 1. Map of western South America and the eastern Pacific ocean floor, showing distribution of large crustal earthquakes, Holocene volcanoes (Simkin and others, 1981), and geologic provinces, relative to the geometry of the subducted Nazca plate (150-km contour on top of Benioff zone shown). Earthquakes shown have magnitudes greater than 5¾ (Gutenberg and Richter, 1954; Rothe, 1969; the *Seismological Notes*, or the *Bulletins of the Seismological Society of America*); those shown with black circles are included in equal-area projections at right (lower hemisphere of common focal sphere) of P, T, and B axes of focal mechanism solutions (Chinn, 1982). Geologic province boundaries are shown by dashed line (eastern limit of recognized Neogene deformation), dash-dotted line (boundary between foreland and hinterland, as defined in text), and light solid line (drainage divide along the Andean crest that also encloses the Altiplano (AL), Puna (P), and Atacama basin (AT)). The trench is mapped by the 6,000-m isobath.
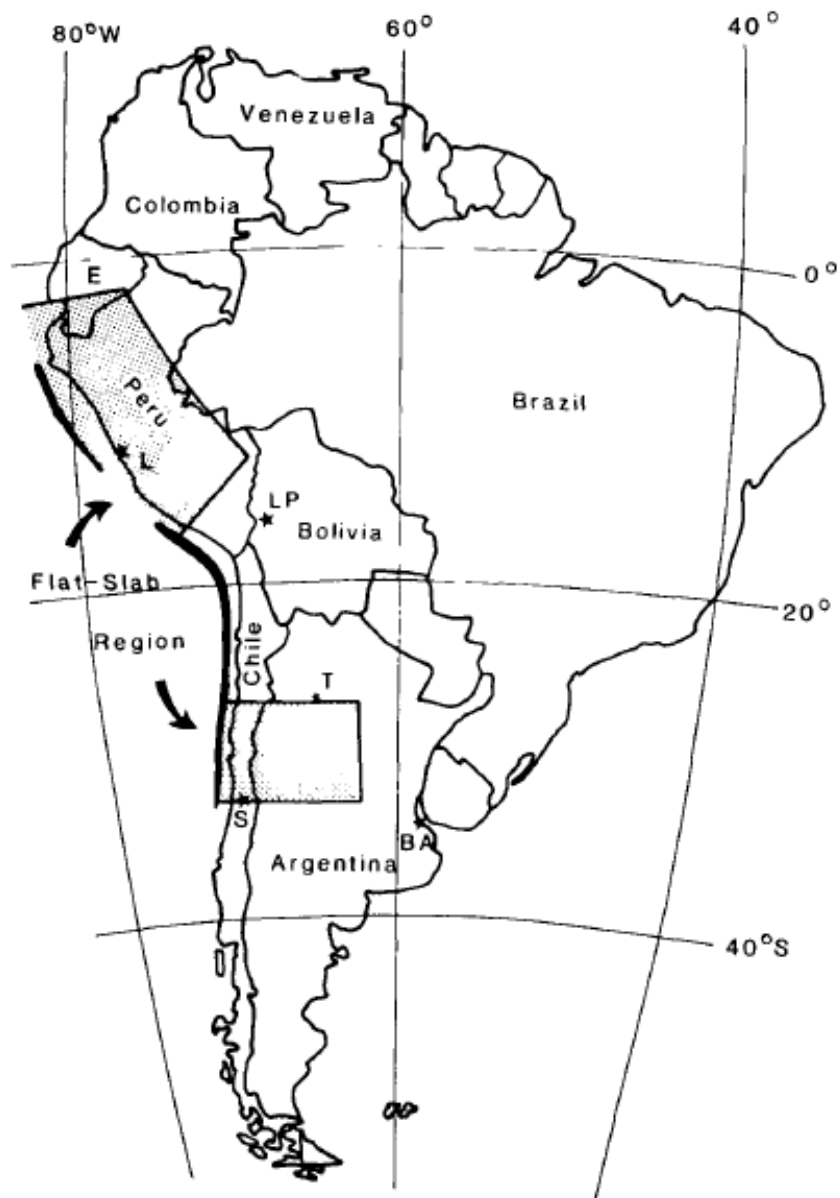
Figure 2. Map of South America, showing locations of sub-horizontal segments of subducted Nazca plate ("flat-slab regions") relative to political boundaries. E, Ecuador; L, Lima; LP, La Paz; T, Tucuman; S, Santiago; BA, Buenos Aires.
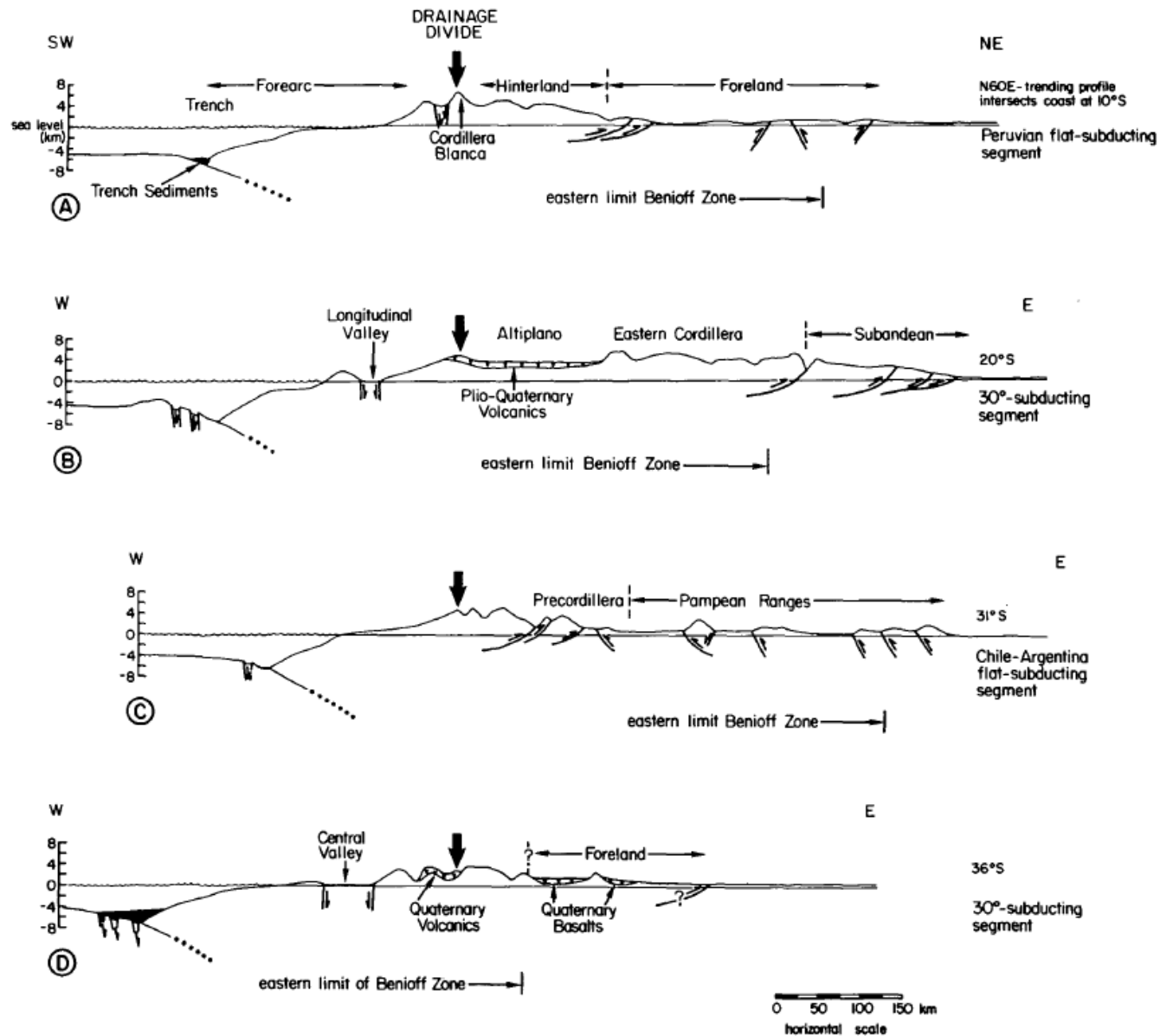
Figure 3. Topographic profiles (about 25 times vertical exaggeration) drawn across Andes perpendicular to tectonic strike, contrasting two regions with nearly horizontal Benioff zone (A, C) with two regions where Benioff zone dips more steeply (B, D). Geometry of Pliocene or Quaternary faults shown schematically. Eastern limit of intermediate depth events of Benioff zone indicated. Compiled from Carte Geologique de l'Amerique du Sud (1964), Operational Navigation Charts (1973), Schweller and others (1981), and references in text.
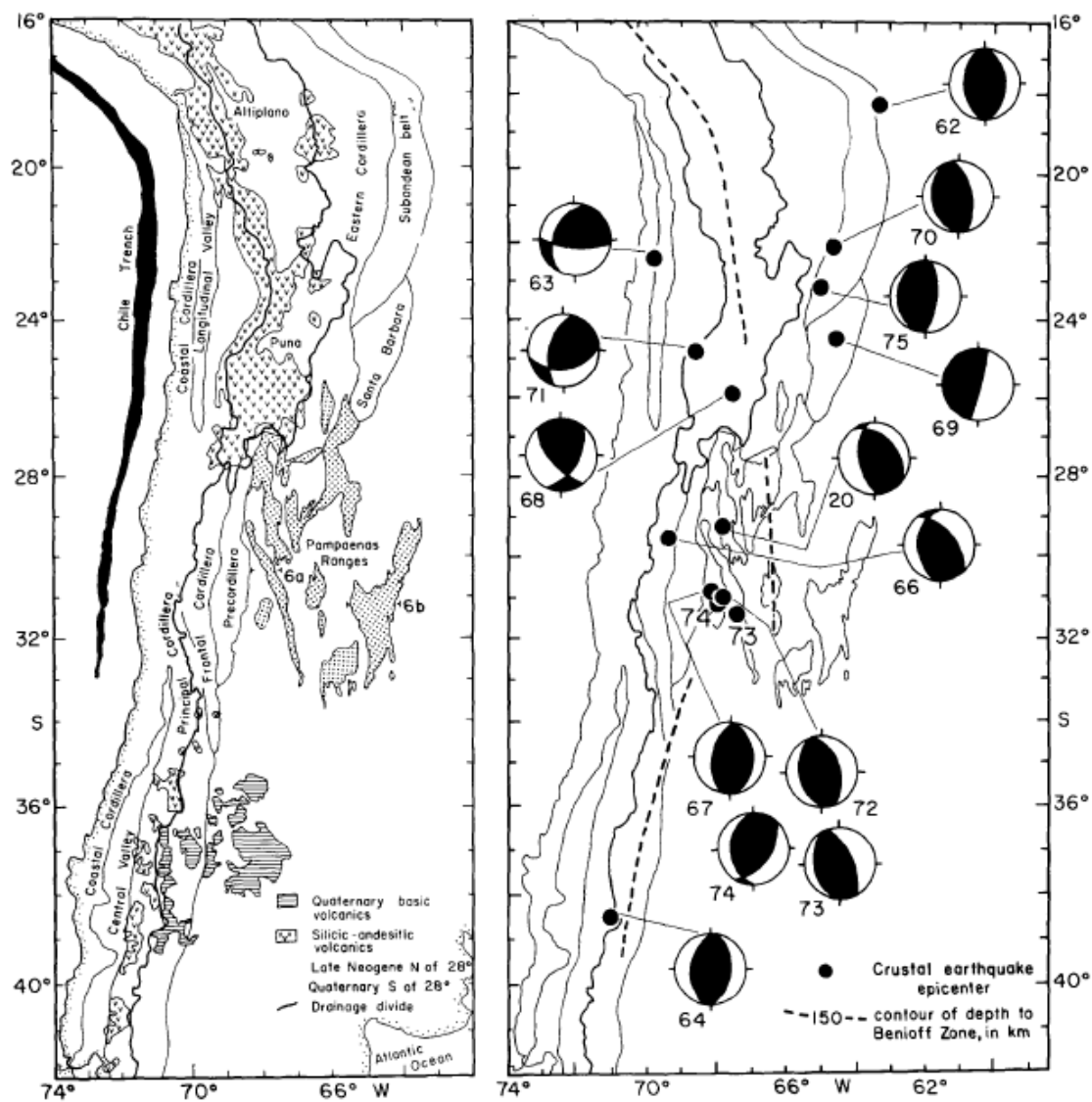
Figure 4. (a) Tectonic provinces and young volcanic cover of the central Andes in Chile, Bolivia, and Argentina. Primary Pacific drainage divide (heavy line) marks Andean crest and forms western boundary of Altiplano-Puna. Eastern boundary of Altiplano-Puna here defined by the divide between the Atlantic Ocean and internal Puna-Altiplano drainage. Trench identified by 6000 m isobath. (From Operational Navigation Charts, 1973; Tectonic Map of South America, 1978; Carte Geologique de l'Amerique du Sud, 1964.) (b) Equal area projections of focal mechanisms for well-determined shallow earthquakes for same area as "a." Numerals beside focal mechanism solutions identify earthquakes listed in Chinn (1982). Flat-slab area between about 28°S and 33°S indicated by eastward shift of 150-km contour on the top of the Benioff zone.
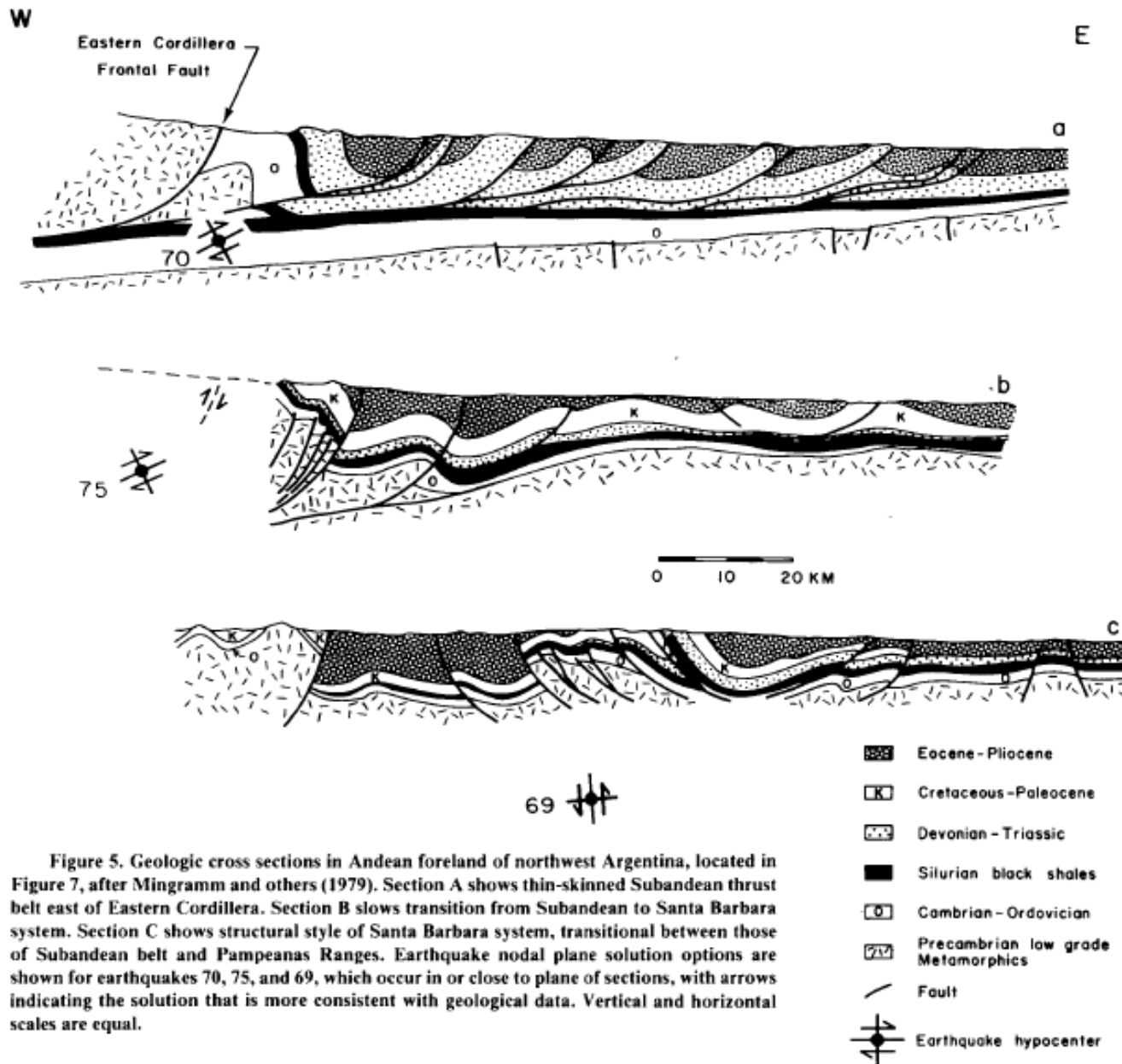
Figure 5. Geologic cross sections in Andean foreland of northwest Argentina, located in Figure 7, after Mingramm and others (1979). Section A shows thin-skinned Subandean thrust belt east of Eastern Cordillera. Section B slows transition from Subandean to Santa Barbara system. Section C shows structural style of Santa Barbara system, transitional between those of Subandean belt and Pampeanas Ranges. Earthquake nodal plane solution options are shown for earthquakes 70, 75, and 69, which occur in or close to plane of sections, with arrows indicating the solution that is more consistent with geological data. Vertical and horizontal scales are equal.
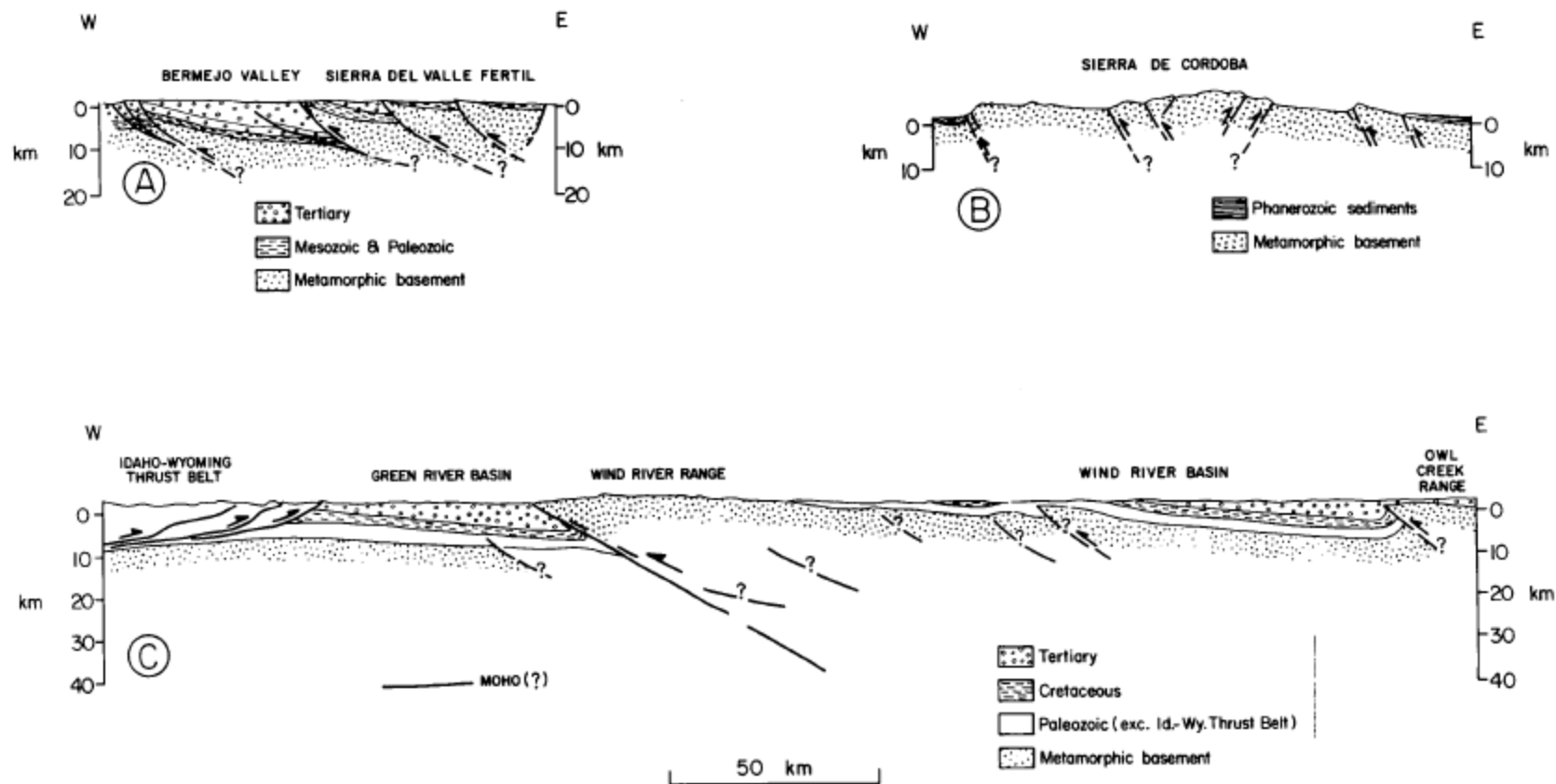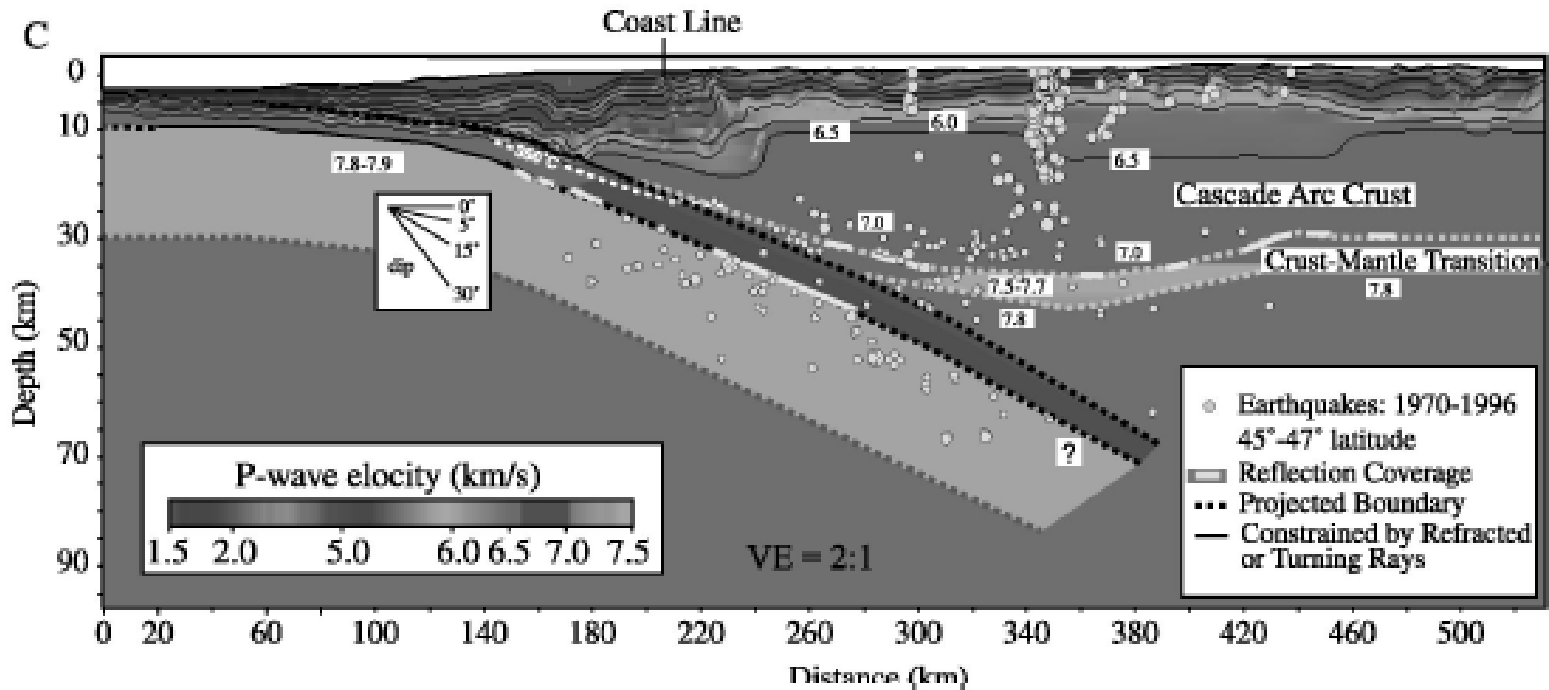
Figure 6. Comparison of structural geometry of uplifts in (A) western and (B) eastern Pampeanas Ranges (located in Fig. 4) to (C) Wind River Mountains in Laramide province of North America (located in Fig. 10). A is from Vasquez and Gorrono (1980), B is from Gordillo and Lencinas (1979), and C is compiled from Royse and others (1975), Case and Keefer (1966), Brewer and others (1980), and Lynn (1980).

thank you!

Coast Line

Figure C. Cross-section showing P-wave velocity structure, earthquake distribution, and crustal boundaries.

The height of the forebulge is thus given by

$$w_b = -\frac{\alpha^2 M_0}{2D} e^{-[(x_b - x_0)/\alpha]} e^{-x_0/\alpha} \frac{\sin\left(\frac{x_b - x_0}{\alpha}\right)}{\cos\left(\frac{x_0}{\alpha}\right)}.$$

(3.158)

Upon dividing Equation (3–157) by Equation (3–158) and eliminating α using Equation (3–156), we obtain

$$\frac{w}{w_b} = \frac{\exp\left[-\frac{\pi}{4}\left(\frac{x - x_0}{x_b - x_0}\right)\right]}{\exp\left(-\frac{\pi}{4}\right)} \frac{\sin\left[\frac{\pi}{4}\left(\frac{x - x_0}{x_b - x_0}\right)\right]}{\sin\frac{\pi}{4}}$$

$$= \sqrt{2} e^{\pi/4} \exp\left[-\frac{\pi}{4}\left(\frac{x - x_0}{x_b - x_0}\right)\right] \sin\left[\frac{\pi}{4}\left(\frac{x - x_0}{x_b - x_0}\right)\right].$$

(3.159)

The plot of w/w_b vs. $(x - x_0)/(x_b/x_0)$ shown in Figure 3–34a defines a *universal flexure profile*. The profile is valid for any two-dimensional elastic flexure of the lithosphere under end loading.
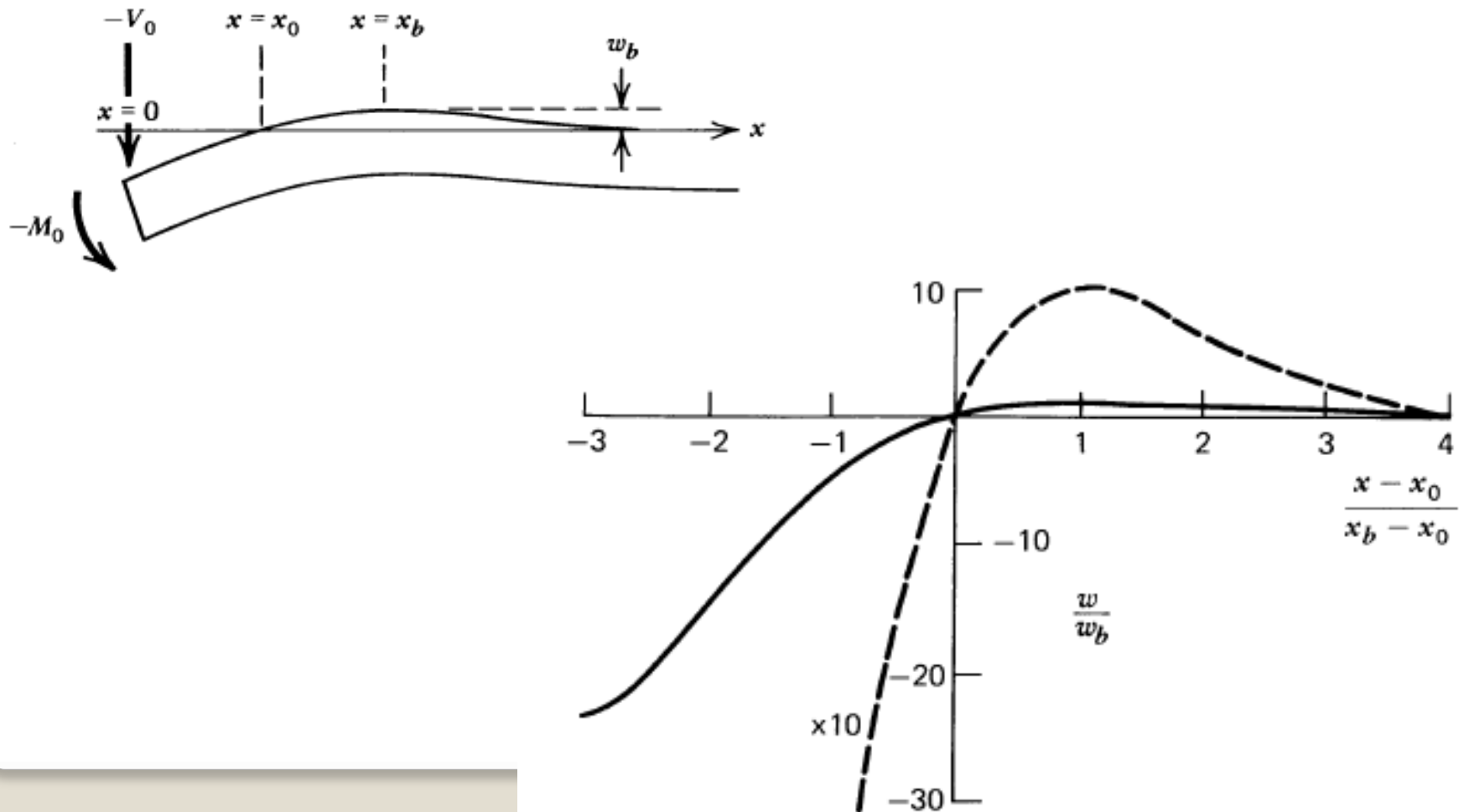
We can solve for the bending moment in terms of $(x - x_0)/(x_b - x_0)$ by substituting Equation (3–159) into Equation (3–73)

$$M = \frac{\sqrt{2}\pi^2 e^{\pi/4}}{8} \frac{Dw_b}{(x_b - x_0)^2} \cos\left[\frac{\pi(x - x_0)}{4(x_b - x_0)}\right] \times \exp\left[-\frac{\pi(x - x_0)}{4(x_b - x_0)}\right].$$
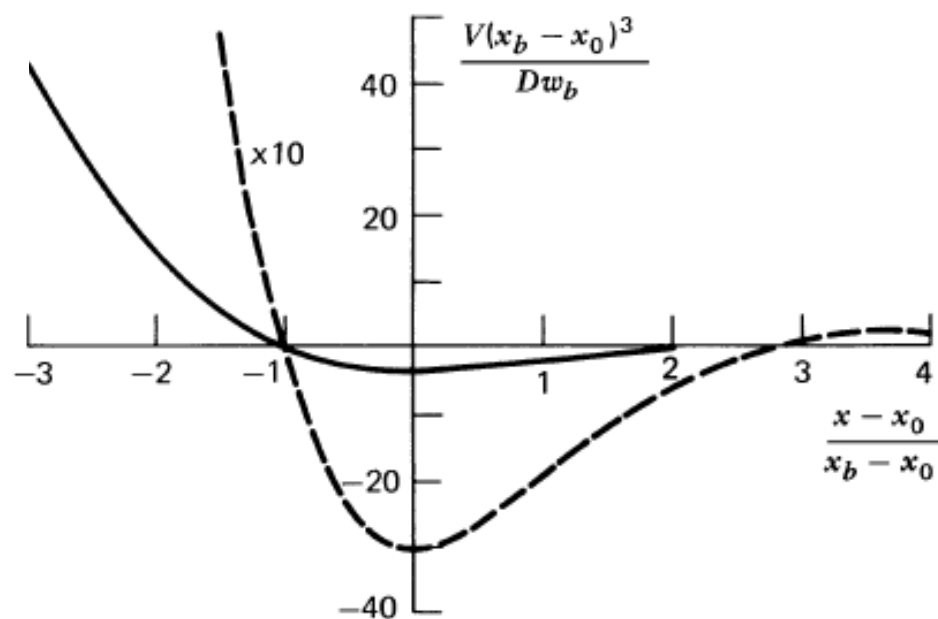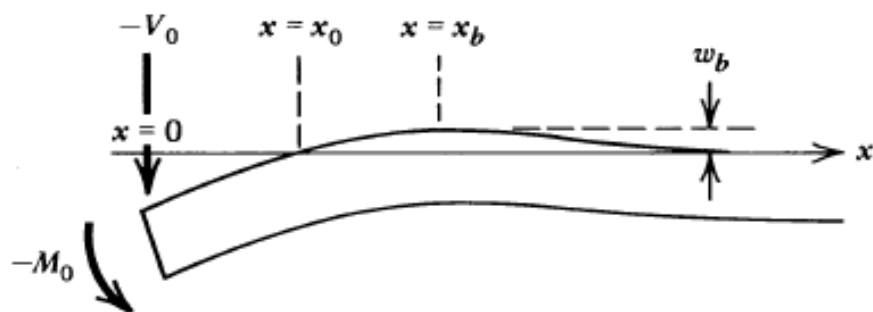
The dependence of $M(x_b - x_0)^2/Dw_b$ on $(x - x_0)/(x_b - x_0)$ is shown in Figure 3–34b. The bending moment is a maximum at $(x - x_0)/(x_b - x_0) = -1$.
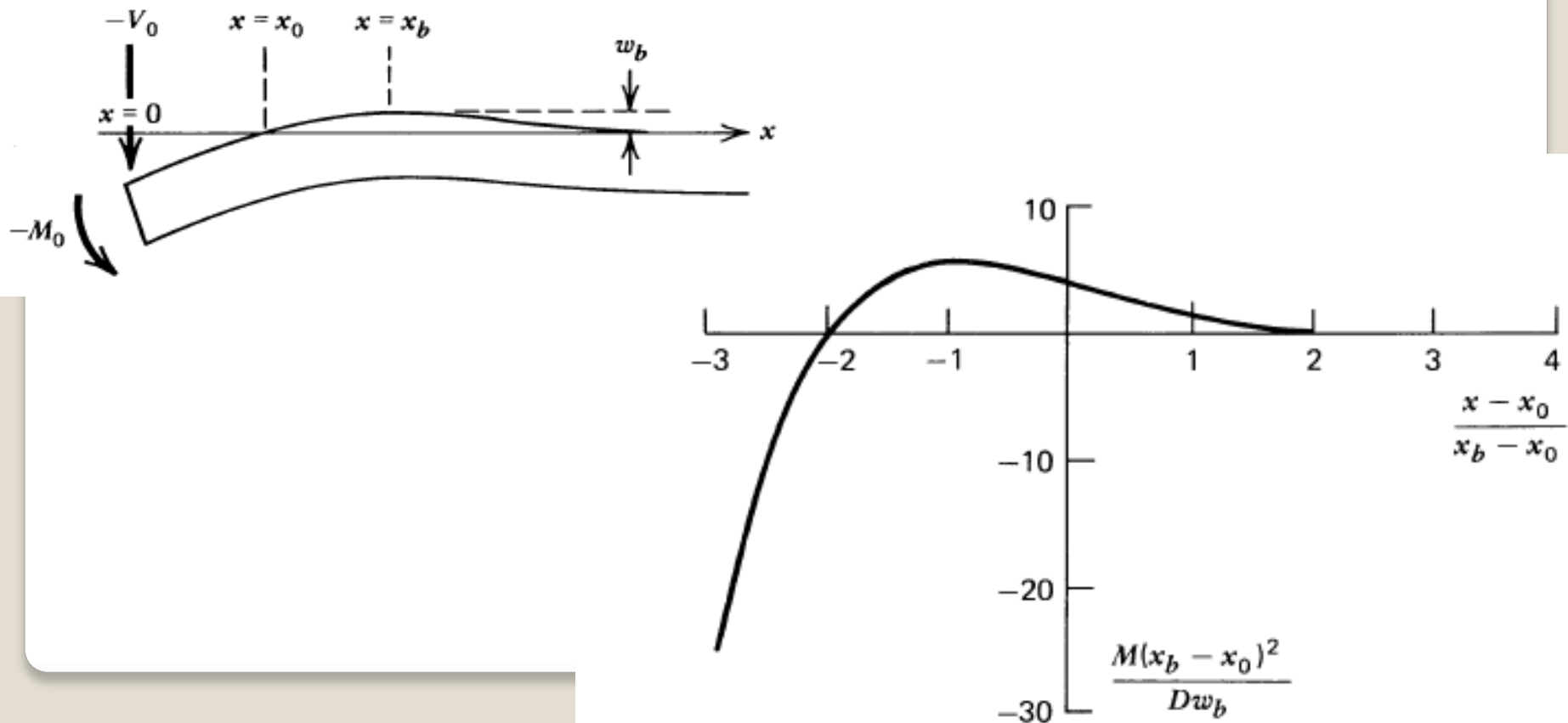
The shear force can be determined from Equations (3–59) and (3–160) to be

$$V = -\frac{\sqrt{2}\pi^3 e^{\pi/4}}{32} \frac{Dw_b}{(x_b - x_0)^3}\left[\cos\left\{\frac{\pi(x-x_0)}{4(x_b-x_0)}\right\}\right.$$

$$\left.+ \sin\left\{\frac{\pi(x-x_0)}{4(x_b-x_0)}\right\}\right] \exp\left[-\frac{\pi(x-x_0)}{4(x_b-x_0)}\right].$$

(3.161)

The dimensionless shear force $V(x_b - x_0)^3/Dw_b$ is plotted vs. $(x - x_0)/(x_b - x_0)$ in Figure 3–34c. The shear force is zero at $(x - x_0)/(x_b - x_0) = -1$.

The universal flexure profile is compared with an observed bathymetric profile across the Mariana trench in Figure 3–35. In making the comparison, we take $x_b = 55$ km and $w_b = 500$ m ($x_0 = 0$). From Equation (3–156) we find that $\alpha = 70$ km. With $\rho_m - \rho_w = 2300$ kg m^{-3} and $g = 10$ m s^{-2}, Equation (3–127) gives $D = 1.4 \times 10^{23}$ N m. From Equation (3–72) with $E = 70$ GPa and $\nu = 0.25$ we find that the thickness of the elastic lithosphere is 28 km. This value is in quite good agreement with the thickness of the oceanic elastic lithosphere obtained by considering island loads. The largest bending stress is 900 MPa, and it occurs 20 km seaward of the trench axis. This is a very large deviatoric stress, and it is doubtful that the near-surface rocks have sufficient strength in tension. However, the yield stress of the mantle is likely to approach this value at depth where the lithostatic pressure is high.

Although the trench bathymetric profile given in Figure 3–35 appears to exhibit elastic flexure, other trench profiles exhibit an excessively large curvature near the point of the predicted maximum bending moment. This is discussed in Chapter 7, where we associate this excess curvature with the plastic failure of the lithosphere.
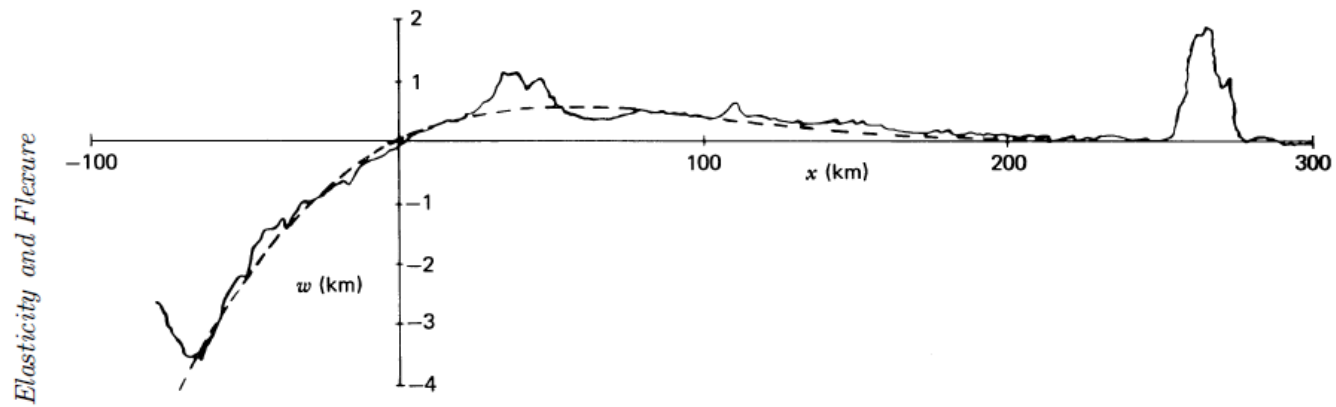
Figure 3.35 *Comparison of a bathymetric profile across the Mariana trench (solid line) with the universal lithospheric deflection profile given by Equation (3–159) (dashed line); $x_b = 55$ km and $w_b = 0.5$ km.*